Modeling of Microporosity, Macroporosity, and Pipe-Shrinkage Formation during the Solidification of Alloys Using a Mushy-Zone Refinement Method: Applications to Aluminum Alloys

Ch. PEQUET, M. GREMAUD, and M. RAPPAZ

A microporosity model, based on the solution of Darcy's equation and microsegregation of gas, has been developed for arbitrary two- (2-D) and three-dimensional (3-D) geometry and coupled for the first time with macroporosity and pipe-shrinkage predictions. In order to accurately calculate the pressure drop within the mushy zone, a dynamic refinement technique has been implemented: a fine and regular finite volume (FV) grid is superimposed onto the finite-element (FE) mesh used for the heat-flow computations. For each time-step, the cells, which fall in the mushy zone, are activated, and the governing equations of microporosity formation are solved only within this domain, with appropriate boundary conditions. For that purpose, it is necessary to identify automatically the various liquid regions that may appear during solidification: *open* regions of liquid are connected to a free surface where a pressure is imposed, *partially closed* liquid regions are connected to an open region *via* the mushy zone, and *closed* regions are totally surrounded by the solid and/or mold. For partially closed liquid pockets, it is shown that an integral boundary condition applies before macroporosity appears. Finally, pipe shrinkage (*i.e.*, shrinkage appearing at a free surface) is obtained by integration of the calculated interdendritic fluid flow over the open-region boundaries, thus ensuring that the total shrinkage (microporosity plus macroporosity and pipe shrinkage) respects the overall mass balance. This very general approach is applied to Al-Cu and Al-Si alloys.

I. INTRODUCTION

POROSITY is one of the major defects in castings, which results in a decrease of the mechanical properties, in particular the fatigue and ultimate tensile strengths.[1] It is induced by two mechanisms, solidification shrinkage and gas segregation, which occur concomitantly but with different intensities.[1–7] Solidification shrinkage, which induces a negative volume variation during the phase transformation of most alloys, has to be compensated for by interdendritic liquid flow (*i.e.*, feeding) to avoid porosity. Feeding induces a pressure decrease in the mushy zone, which combined with a decrease in temperature, lowers the limit of solubility of dissolved gases in the liquid.* In addition, during solidification, the gas rejection at the solid/liquid interface leads to an increased gas concentration in the liquid. If this concentration reaches a critical value, based on the limit of solubility of gas in the liquid, then pores can nucleate and grow (Figure 1). Quantitative information on the development of porosity as a function of alloy variables and casting parameters is particularly important for the foundryman, in order to control and limit the formation of such a defect.

*For some alloys, the pressure might even fall below the vapor pressure of some volatile solute elements (*e.g.,* zinc).

Detailed modeling of microporosity formation has been developed mainly in one-dimensional (1-D) geometry,[2,6,8] occasionally in two dimensions[4,9,10] but rarely in three dimensions.[11,12] Lee *et al.*[13] recently made a fairly extensive review of existing microporosity models for Al-Si alloys. Models were classified according to the proposed approach (analytical, criteria functions, numerical model, *etc.*), and their advantages and drawbacks were pointed out. Recently, Vo *et al.*[14] developed a two dimensional (2-D) axisymmetric model, which is coupled with ABAQUS*. Microporosity predictions are limited to qualitative information because of restrictive assumptions of criteria functions. Sabau and Viswanathan[15] have attempted to solve the equations governing the pressure in the entire liquid and mushy regions, which introduces inherent numerical difficulties: the dynamic pressure in the fully liquid zone (usually smaller than 1 Pa) is significantly lower than the pressure drop in the mushy zone (usually on the order of several KPa). Bounds *et al.*[11] proposed a model for macrodefect predictions based on the coupling of the free-surface flow, heat transfer, and solidification. Numerical schemes for solving the Navier–Stokes equation are complex and convergence may be difficult to obtain. Furthermore, some of the assumptions underlying the physics of microporosity formation are unclear.

*ABAQUS is a registered trademark of Hibbit, Karlsson & Sorenson, Inc., Pawtucket, RI.

On the other hand, pipe shrinkage, *i.e.*, solidification shrinkage appearing at a free surface, and macroporosity, *i.e.*, solidification shrinkage appearing in a closed-liquid pocket (Figure 2(a–b)), can be predicted by most commercial casting software but with information obtained mainly from

Ch. PEQUET, PhD. Student, and M. RAPPAZ, Professor, are with the Institute of Materials, Faculty of Engineering, Ecole Polytechnique Federale de Lausanne, CH-1015 Lausanne, Switzerland. Contact e-mail: michel.rappaz@epfl.ch M. GREMAUD, Managing Director, is with Calcom SA, CH-1015 Lausanne, Switzerland.

Manuscript submitted October 11, 2001.

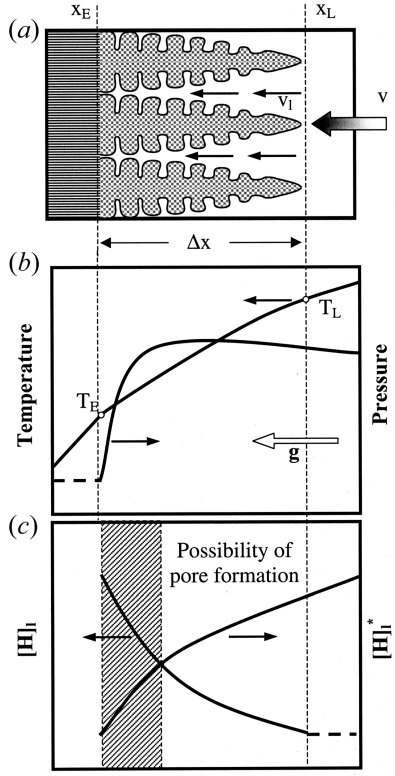

Fig. 1—Schematic representation of (*a*) a 1-D columnar mushy zone; (*b*) temperature and pressure profiles (gravity **g** is toward the left); and (*c*) gas concentration, $[H]_l$, and gas solubility limit in the liquid, $[H]_l^*(T, p, c_l)$.

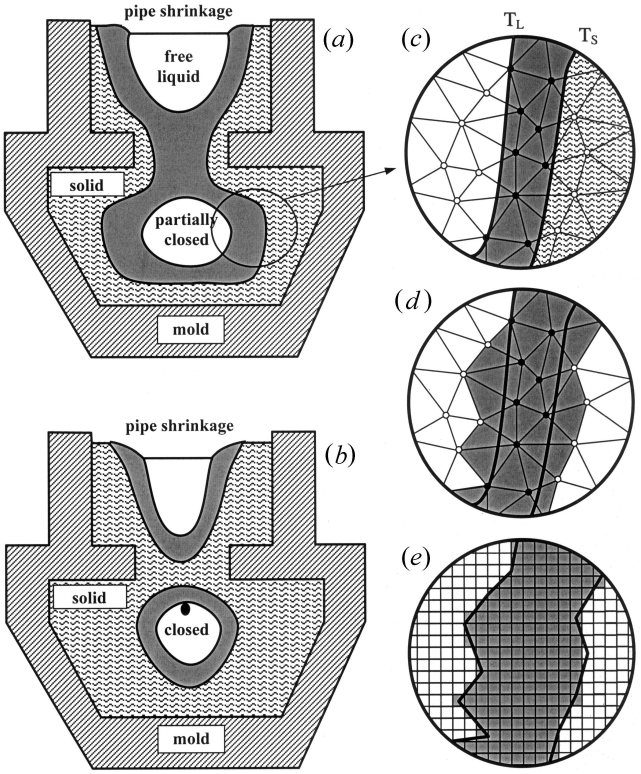

Fig. 2—(*a*) Schematic representation of pipe shrinkage at a top free surface and of a partially closed liquid pocket. (*b*) A macropore, which might start to form in a partially closed liquid region (black area) when this liquid region is closed. (*c*) A magnified view of the mushy zone shows that only few FE nodes fall within its thickness (filled circles). (*e*) The FE elements are refined into small regular squares or cells (*a*), and those falling within mushy elements (gray elements in (*d*)) are activated.

the thermal field. Up to now, such calculations have never been coupled with microporosity prediction in a consistent way. Moreover, the transition between open regions of liquid (*i.e.*, liquid regions connected to a free surface) and closed regions (*i.e.*, liquid regions totally surrounded by the solid or the mold) has never been taken into account. At some stage, a liquid region may become totally surrounded by the mushy zone but not by the solid: for such partially closed liquid pockets, feeding can still occur *via* the mushy zone.

The accuracy is another problem arising in microporosity prediction for geometry other than 1-D. One of the main advantages of unstructured meshes (typical of the finite-element (FE) method) over structured ones (typical of the finite-difference (FD) method)* is that fewer elements and nodes are required to accurately describe the geometry and solidification of complex cast parts.[16] However, as a consequence, fewer nodes are also present across the mushy zone to calculate the pressure drop and microporosity formation. On the other hand, structured meshes used to calculate solidification in complex geometry are fine everywhere: this drastically increases the total number of nodes and central processing unit (CPU) time, without necessarily producing enough nodes across the mushy zone.

Although the present contribution is based on a fairly classical approach of porosity modeling, first initiated by Piwonka and Flemings,[2] it introduces several new concepts. First, in order to keep the advantages of unstructured meshes while improving the accuracy in the mushy zone, a mushy-zone refinement technique has been developed (Section II). The volume elements of the refined grid (hereafter, called cells)* are activated as the mushy zone moves across the coarse unstructured mesh, and the equations governing microporosity formation are solved only for those cells. Second, since the governing equations of the problem, which are presented in Section III, are only solved in the refined mushy region, conditions must be defined at the boundaries of this zone (Section IV). For that purpose, it is necessary to distinguish the nature of various liquid pockets that may form during solidification (open, partially closed, and closed). It is shown that an integral boundary condition (IBC) applies for partially closed liquid pockets. In Section V, the numerical method is briefly described, whereas numerical results validating the method and showing the influence of various parameters are presented in Section VI. Although the method is mainly applied to aluminum alloys, it is generally valid and can be easily extended to other systems.

*The so-called finite-volume (FV) method can be based on either structured or unstructured meshes.

*This denomination of "cell" is introduced to clearly distinguish an element of the refined structured grid from an element of the unstructured coarse mesh (called element).

II. MUSHY-ZONE REFINEMENT TECHNIQUE

In the present approach, it is assumed that macroscopic phenomena occurring at the scale of the whole casting, such

as heat and mass transfer, can be described using a fixed and coarse unstructured mesh. A FE method formulation of the average conservation equation is applied, but equivalent methods based on unstructured meshes, such as FV method, work as well. However, at any given time-step, the mushy zone, Ω_{sl}, may only occupy a small fraction of the whole domain, Ω, occupied by the metal (volume, V_Ω) (Figure 2). This is particularly true for alloys solidifying with a short solidification interval, ΔT_o, in a strong thermal gradient, G. In order to accurately describe the pressure drop and microporosity formation in such a zone, a refinement of this zone rather than an adaptive grid method[17] is selected because it is much simpler to implement, especially for three-dimensional (3-D) geometry, and is much faster. On the other hand, this approach is close to that previously used for the modeling of grain structure formation (Cellular Automation-Finite Element (CAFE) model[18]), and therefore, some existing numerical tools could be adapted to our needs. In the present case, the cell size, a, of the fine grid is not directly connected to the microstructure (*e.g.*, secondary dendrite-arm spacing as in the CAFE model) but is dictated by the required number of nodes across the mushy zone, N_{sl}, along the thermal gradient (typically 10 to 10^2). If $G_{\max}$ is the maximum thermal gradient in the casting and ΔT_o is the solidification interval, a is given by

$$a = \frac{\Delta T_0}{G_{\max}} \frac{1}{N_{sl}} \qquad [1]$$

The total number of cells in the casting is, therefore, equal to $V_\Omega a^{-d}$, where d is the dimensionality of the problem (2 or 3).

The fine and regular FV grid, covering the whole domain Ω filled with metal, is generated and superimposed onto the FE mesh prior to the calculations (Figure 2). For each element to which they belong, the cells are numbered in a sequential order according to a scan in the x-, y-, and possibly z-directions. Since the mushy zone, $\Omega_{sl}(t)$, evolves with time, only those cells located in the mushy elements must be activated at a given time. An element (e) is considered to be mushy when its temperature interval, $[\min T, \max T]_{(e)}$, defined by the minimum and maximum temperatures of all its nodes, overlap the solidification interval defined by the liquidus temperature, T_L, and the solidus or eutectic temperature, T_S/T_E.

The number of activated cells during one time-step, N_c, is of the order of $N_{sl}\,(V_\Omega)^{(d-1)/d}\,a^{(1-d)}$ if the gradient is fairly strong (*i.e.*, $\Delta T_o G^{-1} < (V_\Omega)^{1/d}$) or $(V_\Omega a^{-d})$ if the whole casting is mushy. During solidification, an inactive cell can become active, while an active cell can remain active or become inactive.

III. MICROPOROSITY MODEL

As in most previous works,[2,4,6,8–10] the present model of microporosity formation is based on two main phenomena: pressure drop in the mushy zone, on one hand, and segregation of gas/precipitation of gas bubbles (cavitation), on the other.

A. *Pressure Drop in the Mushy Zone*

The motion of liquid metal in the mushy zone is supposed to be governed by the pressure field only (in the absence of pores). The local pressure in the liquid, $p_l(\mathbf{x}, t)$, is made of several components:

$$p_l = p_a + p_m + p_d \qquad [2]$$

where p_a is the atmospheric (or external) pressure, p_m is the metallostatic contribution, and p_d is the dynamic contribution responsible for the movement of the liquid in the mushy zone (not to be confused with the much smaller dynamic pressure in fully liquid regions). In Figure 1, the negative slope of the pressure profile close to the dendrite tips is due to gravity (*i.e.*, slope of p_m), whereas the contribution of p_d is clearly visible near the roots of the dendrites. Assuming that Darcy's equation describes the flow in the mushy region, the superficial velocity of the interdendritic liquid, $\mathbf{v}(\mathbf{x}, t)$, is given by

$$\mathbf{v} = -\frac{K}{\mu}\,\mathbf{grad}\,p_d = -\frac{K}{\mu}\,[\mathbf{grad}\,p_l - \rho_l \mathbf{g}] \qquad [3]$$

where K is the permeability of the solid skeleton, μ is the dynamic viscosity of the liquid, ρ_l is its specific mass, and $\mathbf{g}$ is the gravity vector. The dynamic viscosity is expressed as a function of temperature, T,

$$\mu = \mu_0 \exp\left[\frac{E_\mu}{RT}\right] \qquad [4]$$

Here, μ_0 is the viscosity at very high temperature, E_μ is an activation energy, and R is the universal gas constant. The permeability, K, which reflects the resistance of the solid pattern to the fluid flow, has been deduced here from the Kozeny–Carman's equation:[8]

$$K(g_s(t), \lambda_2(t)) = \frac{(1 - g_s(t))^3}{g_s(t)^2}\,\frac{\lambda_2^2(t)}{180} \qquad [5]$$

where $g_s(t)$ is the volume fraction of solid, and $\lambda_2(t)$ is the secondary dendrite-arm spacing, which may be evaluated at any point of the mushy zone using a coarsening law:[19]

$$\lambda_2(t) = \left[\lambda_{2,0}^3 + M(t)(t - t_L)\right]^{1/3} \quad \text{with} \qquad [6]$$

$$M(t) = \frac{\sigma_{sl} D_l T_M}{L(1-k)m}\,\frac{\ln c_l(t) - \ln c_{l,0}}{c_l(t) - c_{l,0}}$$

$\lambda_{2,0}$ is the arm spacing before ripening (*i.e.*, close to the dendrite tips), which is assumed to be equal to twice the tip radius. The M term is the coarsening factor (written here for a binary alloy, but similar law can be deduced for a multicomponent system[20]). The time, t_L corresponds to the instant when the temperature reaches the liquidus (*i.e.*, beginning of solidification), and thus, $(t - t_L)$ is the time elapsed since the local temperature became lower than the liquidus. The parameters of this coarsening factor are the interfacial solid-liquid energy, σ_{sl}; the diffusion coefficient of solute in the liquid, D_l; the melting point of the pure system, T_M; the volumeric latent heat of fusion, L; the partition coefficient, k; the slope of the liquidus, m; and the current and the nominal concentration of solute in the liquid, $c_l(t)$ and $c_{l,0}$, respectively. Consequently, the coarsening factor is also a function of time.

B. *Mass Conservation*

Assuming that the solid phase is not moving and that there is no deformation[21] and, furthermore, neglecting the

specific mass of the bubbles, the average conservation equation of mass written for both phases gives

$$\frac{\partial}{\partial t}\left[\rho_s g_s + \rho_l g_l\right] + \text{div}\left(\rho_l g_l \mathbf{v}_l\right) = 0 \qquad [7]$$

where ρ_s is the specific mass of the solid, and $\mathbf{v}_l$ is the effective velocity of the fluid between the solid skeleton (*i.e.*, $\mathbf{v} = g_l \mathbf{v}_l$). If porosity formation has already occurred, the volume fraction of liquid, g_l, is given by:

$$g_l = 1 - g_s - g_p \qquad [8]$$

where g_p is the volume fraction of pores. Combining Eqs. [3], [7], and [8], one gets

$$\text{div}\left[-\rho_l \frac{K}{\mu}\left(\mathbf{grad}\, p_l - \rho_l \mathbf{g}\right)\right] - \rho_l \frac{\partial g_p}{\partial t} = \qquad [9a]$$

$$-\left(\rho_s - \rho_l\right)\frac{\partial g_s}{\partial t} - \left(1 - g_s - g_p\right)\frac{\partial \rho_l}{\partial t} - g_s \frac{\partial \rho_s}{\partial t}$$

In other words, solidification shrinkage and specific mass variations, respectively, the first and two last terms on the right-hand side (RHS) of Eq. [9a], can be compensated for by feeding (the first term on the left-hand side (LHS)) and/or by microporosity formation (the second term on the LHS). The RHS terms are supposed to be known from a heat-flow computation (including fluid flow in the liquid region or not) and from the knowledge of the specific mass of the solid and of the liquid phases. Since the product of the fraction of porosity and variation of the specific mass of the liquid is second-order, Eq. [9a] can also be written as:

$$\text{div}\left[-\rho_l \frac{K}{\mu}\left(\mathbf{grad}\, p_l - \rho_l \mathbf{g}\right)\right] - \rho_l \frac{\partial g_p}{\partial t} = \qquad [9b]$$

$$-\frac{\partial \langle\rho\rangle_0}{\partial t} = -\frac{d\langle\rho\rangle_0}{dT}\frac{\partial T}{\partial t}$$

where $\langle\rho\rangle_0 = (\rho_s g_s + \rho_l(1 - g_s))$ is the average mass of the solid-liquid mixture without porosity. This value could be measured for example by densitometric measurements or calculated by using a solidification model for $g_s(T)$ and knowing the specific mass (also possibly a function of T) of each individual phase. In many alloys, the variations of specific mass in the liquid are much more pronounced than that in the solid[22] because of the fact that the partition coefficients, k_i, are usually much smaller than unity. The term ρ_l can be written as

$$\rho_l = \rho_{l,0}\left[1 - \beta_T(T - T_0) - \beta_c(c_l - c_{l,0})\right] \qquad [10]$$

where $\rho_{l,0}$ is a reference specific mass of the liquid taken at the nominal temperature, T_0, and liquid composition, $c_{l,0}$. The terms β_T and β_c are the thermal and solutal expansion coefficients, respectively. The specific mass of the primary solid phase, ρ_s, can be considered as constant until a eutectic reaction occurs (specific mass of the eutectic, $\rho_e \neq \rho_s$).

As can be seen, two scalar fields appear in Eq. [9]: the pressure in the liquid, $p_l(\mathbf{x}, t)$, and the volume fraction of microporosity, $g_p(\mathbf{x}, t)$. This elliptic-type equation can be solved, provided appropriate boundary conditions are given for the pressure (Section IV), and these two fields are coupled *via* a supplementary equation of state. In the case of aluminum alloys, this additional equation is furnished by the segregation and precipitation of hydrogen.

C. *Hydrogen Mass Balance*

In most metallic alloys, there is a certain amount of gas dissolved in the liquid or of solute elements having a fairly high vapor pressure. Since the present contribution focuses on aluminum alloys, we will consider in the following the segregation of one gas species only, namely, hydrogen and neglect the influence on porosity formation of other elements, such as zinc*

*At 730 °C, the vapor pressure of zinc is 13 kPa.

1. When no pore has formed. Yet at a given location ($g_p = 0$), there is only one variable, the pressure, appearing in Eq. [9], and the problem is well defined. Assuming lever-rule and a locally closed system for the segregation of such a gas, the mass balance of hydrogen can be written, in this case, as

$$[\text{H}]_0\rho_l = [\text{H}]_s\rho_s g_s + [\text{H}]_l\rho_l(1 - g_s) \qquad \text{if } g_p = 0 \qquad [11]$$

where $[\text{H}]_0$ is the nominal concentration of hydrogen in the melt, and $[\text{H}]_s$ and $[\text{H}]_l$ are the hydrogen concentrations in the solid and liquid, respectively. These last two concentrations are assumed to be related by the partition coefficient k_H, *i.e.*, $[\text{H}]_s = k_\text{H}[\text{H}]_l$, taking this value as equal to that of the saturated solutions (*i.e.*, given by Sieverts' law). Equation [11] then allows one to directly calculate the effective concentration in the liquid, $[\text{H}]_l(g_s)$, as a function of the volume fraction of solid only.

2. As soon as porosity formation occurs. Hydrogen (or gas) conservation can be written as

$$[\text{H}]_0\rho_l = [\text{H}]_s\rho_s g_s + [\text{H}]_l\rho_l(1 - g_s - g_p) \qquad [12]$$

$$+ \alpha\frac{g_p p_p}{T} \qquad \text{if } g_p \neq 0$$

α is a gas conversion factor, p_p is the pressure in the pores, and T is the temperature (in K). The gas concentrations in each phase are given by Sieverts' law:

$$[\text{H}]_s^*(T, p_p, c_l) = S_s(T, c_s)\sqrt{\frac{p_p}{p_0}} \qquad \text{and}$$

$$[\text{H}]_l^*(T, p_p, c_l) = \text{S}_\text{l}(T, c_l)\sqrt{\frac{p_p}{p_0}} \qquad [13a]$$

where S_s and S_l are the temperature and solute-dependent equilibrium constants, p_0 is the standard pressure, and c_l is the solute concentration per unit mass. Sieverts' constant for the liquid, $\text{S}_\text{l}(T, c_l)$, is correlated with temperature and composition of the liquid by the use of the following relationship:[7]

$$\text{S}_\text{l}(T, c_l) = \frac{1}{K_1 f_H}$$

$$\text{with } \ln K_1 = \frac{5872}{T} + 3.284 \text{ and } \log_{10} f_H = e_H^{cl}\, c_l + r_H^{cl} c_l^2 \qquad [13b]$$

where e_H^{cl} and r_H^{cl} are interaction solute coefficients on hydrogen of the first and second order.

The concentrations in the liquid and solid phases are given by the pressure in the existing pores and not in the liquid, since the "reservoir" of gas (*i.e.*, the bubbles) with which these two phases are assumed to be in equilibrium is curved. The pressure in the pores is given by

$$p_p = p_l + \Delta p_r \quad [14]$$

where Δp_r is the overpressure due to the capillarity effect. The radius of curvature of the pore being r (refer to section III–D), Δp_r is given by Laplace's law:

$$\Delta p_r = p_p - p_l = \frac{2\,\sigma_{lg}}{r} \quad [15]$$

where σ_{lg} is the interfacial tension between the liquid and the pore (gas), which is not to be confused with the interfacial energy, σ_{sl}, between the solid and the liquid (Eq. [6]).

D. *Nucleation Criterion and Growth Law of Pores*

As for the formation of a primary phase, pores must nucleate in a supersaturated liquid (cavitation) in order to overcome the curvature contribution. Three concomitant phenomena lead to a supersaturation in gas of the interdendritic liquid phase:[1] increase of $[H]_l$ due to segregation, pressure drop due to feeding, and temperature decrease. When $[H]_l$ exceeds, by a certain amount, the equilibrium value given by Sieverts' law, $[H]_l^*(T, p_l, c_l)$ (Figure 1), pores are assumed to nucleate with a given and fixed density, n_0**.

**The present model of nucleation is, therefore, equivalent to setting a Dirac function of weight, n_0, at the supersaturation, $[\Delta H]_l^n$. As compared with more sophisticated nucleation models used in formation of solid phases,[23] this can be viewed as a Gaussian distribution of zero standard deviation, *i.e.*, all nucleation sites becoming active at a unique supersaturation.

Defining the supersaturation for nucleation as $[\Delta H]_l^n$, pores will form if

$$[H]_l(g_s) \geq [H]_l^*(T, p_l, c_l) + [\Delta H]_l^n \quad [16]$$

In fact, $[\Delta H]_l^n$ can be converted into a critical radius of curvature of the pore nucleus, r_0, by writing $[H]_l^*(T, p_l, c_l) + [\Delta H]_l^n = [H]_l^*(T, p_p, c_l)$, thus allowing to find p_p *via* Eq. 15. Since pore nucleation is heterogeneous in nature (*i.e.*, significantly large value of r_0 and small value of $[\Delta H]_l^n$), the presence of a nonwetting phase in the liquid, such as oxide particles,[1] is required (Figure 3).

In gas porosity,[1] pores can be considered as spherical, since they appear at an early stage of solidification and are not too much constrained by the solid network. Consequently, Eq. 15, applied during the entire growth of the pores, allows the deduction of the pressure field, p_l, and the fraction of porosity field, g_p. However, initial nucleation and growth of pores in a constraining network of well-developed dendrites, require to describe an average radius of the curvature of the pores. The complete growth of a pore, from the instant of heterogeneous nucleation until the last growth stage when the pore morphology is constrained by the secondary dendrite arms, is shown schematically in Figure 3. In such cases, the radius of nucleation, r_0, is kept constant until the volume fraction of pores corresponds to spherical pores. From that instant, the average radius of curvature is a function of the volume fraction of solid, g_s, and of the secondary dendrite-arm spacing, λ_2, in order to express the increasing difficulty for the pores to grow in between the dendritic network (*i.e.*, "pinching" effect). The evolution of this radius of curvature is assumed to be given by

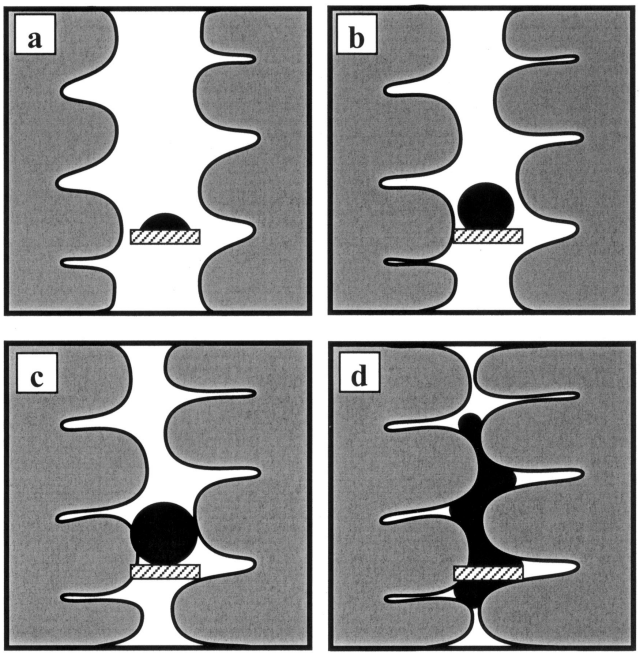

Fig. 3—Various stages of a pore development: (*a*) just after nucleation on an oxide particle/inclusion, (*b*) during initial growth (constant radius), (*c*) later during growth (variable radius), and (*d*) when it is constrained by the dendrite arms.

$$r(g_s, \lambda_2) = \max\left[r_0; \min\left\{\left(\frac{3g_p}{4\pi n_0}\right)^{1/3}; \frac{\lambda_2}{2}\frac{(1-g_s)}{g_s}\right\}\right] \quad [17]$$

$$\text{until } g_s = (1 - g_e)$$

where g_e is the final volume fraction of eutectic after solidification.

IV. BOUNDARY CONDITIONS

Since the coupled Darcy- and mass-conservation equations must normally be solved only in the mushy zone, it is necessary to introduce conditions at all the boundaries of this region. In previous articles dealing with microporosity formation, such computations were extended in the solid and liquid phases by using a penalty method, *i.e.*, by setting a very small, respectively large, permeability. However, as shown by Ampuero *et al.*,[6] special care has to be taken for the boundary condition imposed on the eutectic front growing in between the dendrites in order to respect mass conservation and predict accurately the pressure field.

In the present mushy-zone refinement technique, it is also essential to define appropriate boundary conditions at all the boundaries. As illustrated in Figure 2, it is, therefore, necessary to first distinguish the nature of the remaining liquid regions that can be present in a casting. A region of liquid is a continuous portion of the solidifying domain where only the liquid phase is present. It can be one of the following.

(1) ***Open*** if a portion of its boundary is in direct contact with another medium (usually a gas) for which a pressure can be defined (free surface). Such regions act as feeders of the mushy zone, and thus, their upper level can be lowered during solidification (*i.e.*, formation of pipe shrinkage, Figure 2).
(2) ***Partially closed*** if it is totally surrounded by a mushy zone, which is connected to an open-liquid region (*i.e.*, this zone can still be fed by some liquid flowing from an open region of liquid).
(3) ***Closed*** if it is totally surrounded by a mushy zone, which is surrounded by the solid or the mold.

The boundary conditions applied on the various boundaries are as follows (Figure 4).

(1) For an open-liquid region, a Dirichlet condition is imposed for the pressure at the liquidus front:

$$p_l = p_a + p_m = p_a + \rho_l g h \qquad [18]$$

where p_a and p_m are the atmospheric and metallostatic pressures, respectively h being the height separating the free surface and the actual position of the liquidus front.

(IIa) As long as the eutectic phase has not yet appeared at the surface of the mold (situation not represented in Figure 4), the condition to be applied at the roots of the dendrites is that of a zero velocity in the liquid. Using Darcy's equation, this is equivalent to a Neumann condition for the pressure field:

$$v_{l,n} = 0 \quad \text{or} \quad \frac{\partial p_l}{\partial n} - \rho_l g_n = 0 \qquad [19]$$

where **n** is the unit normal to the boundary, pointing outward of the mushy zone and $g_n = \mathbf{g} \cdot \mathbf{n}$.*

*This boundary condition is equivalent to assuming that the oxide skin at the surface prevents the interdendritic liquid from flowing in between the dendrite arms. Another possibility would have been to assume some (unknown) flow from the surface by setting a Dirichlet condition, $p = p_a + \Delta p_{\text{meniscus}}$, where $\Delta p_{\text{meniscus}}$ is a (negative) curvature contribution associated with the concave shape of the liquid surface in between dendrite arms. The calculated flow at the surface would then have been used to calculate surface porosity in a way similar to (IIIb).

(IIb) At the dendrite roots, the formation of a eutectic imposes the following mass balance,[6]

$$v_{l,n} = -\left[\frac{\rho_e}{\rho_l} - 1\right] v_{e,n} \qquad [20]$$

if no microporosity has formed. The term $v_{e,n}$ is the normal component of the eutectic front velocity, and ρ_e is the average specific mass of the eutectic. Using Darcy's equation, this condition gives a Neumann condition again:

$$\frac{\partial p_l}{\partial n} - \frac{\mu}{K} g_l \left[\frac{\rho_e}{\rho_l} - 1\right] v_{e,n} - \rho_l g_n = 0 \qquad [21]$$

Condition [20] would normally imply the use of a front-tracking method at the eutectic/liquid interface (due to the presence of $v_{e,n}$). Instead of this, a penalty method, developed by Ampuero *et al.*,[6] has been used to account for this condition on a fixed grid. It is equivalent to: (a) spreading the eutectic reaction over a few time-steps (this is the case anyhow with an enthalpy formulation of the heat-flow equation); (b) keeping the permeability constant during the eutectic reaction and equal to the value calculated at the onset of this reaction, *i.e.*, $K = K(1 - g_e)$; and (c) setting the normal velocity of the fluid equal to zero at the end of the eutectic reaction (*i.e.*, when $g_s = 1$). In the case of a 1-D geometry, Ampuero *et al.*[6] showed that this penalty method gives values very close to those obtained with a front-tracking technique.

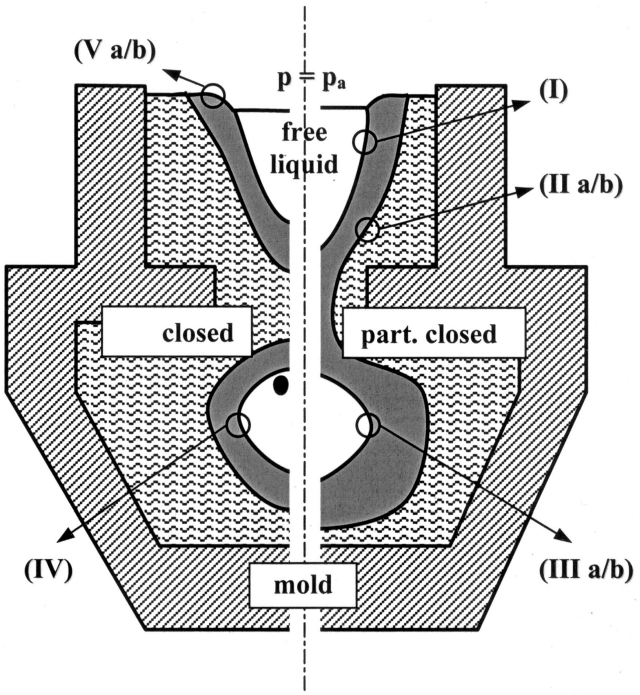

Fig. 4—Boundary conditions applied at the boundary of the mushy zone for (I) the liquidus front of an open region of liquid, (II) the root of the mushy zone, (III) the liquidus front of a partially closed liquid pocket, (IV) the liquidus front of a closed liquid pocket, and (V) the free surface.

(IIIa) For a partially closed liquid pocket and as long as no macropore has formed in such region, an IBC must be prescribed along the liquidus front. The pressure, p_Q, at some point, Q, of the boundary is set to an *a priori* unknown value, which must satisfy the following integral mass balance:

$$\int_{\Omega_l} \text{div}(\rho_l \mathbf{v}_l)\, dV = \int_{\partial\Omega_l} \rho_l \mathbf{v}_l \cdot \mathbf{n} dS = 0 \qquad [22]$$

where $\partial\Omega_l$ is the boundary of the partially closed liquid pocket, and **n** is its unit normal pointing outward of the mushy zone. The values at the other points of the boundary are then given by $p = p_Q + \rho_l g h$, where h is the height separating this point and Q. In order to predict macropore formation in such a partially closed liquid pocket (IIIb), point Q is chosen as the highest location (with respect to gravity) of this region (lowest value of p_Q).

(IIIb) For a partially closed liquid pocket, when the pressure p_Q falls below a cavitation pressure, p_c, a macropore forms. If nucleation of a macropore is neglected, this pressure, p_c, is directly given by Sieverts' law Eq. [13], calculated with the corresponding solute concentration and temperature. In such a case, the pressure

is then prescribed (*i.e.*, $p_Q = p_0\,[\mathrm{H}]_0^2\,\mathrm{S_l}(T,c_{l,0}))^{-2}$) at point Q and the mass balance, Eq. [22], is no longer satisfied. The growth rate of the macropore volume, V_p, is directly given by

$$\frac{dV_p}{dt} = -\int_{\partial\Omega_l} \mathbf{v}_l \cdot \mathbf{n}\, dS \qquad [23]$$

Please note that the concentration of gas in the remaining liquid should normally be recalculated at each time-step according to a mass balance similar to Eq. [12] in order to account for the amount of gas in the macropore and to update the cavitation pressure with $p_0\,[\mathrm{H}]_l^2\,\mathrm{S_l}(T, c_l)^{-2}$. However, considering all the other assumptions, the cavitation pressure is kept to the value given by Sieverts' law for $[\mathrm{H}]_0$.

(IV) Closed-liquid regions are treated exactly as partially closed ones in which a macropore has already formed (*i.e.*, boundary condition (IIIb)). The only difference is that the algorithm automatically prevents any liquid to flow in such regions, *i.e.*, the closed-liquid pocket and its surrounding mushy zone constitute a closed system.

(V) At the boundary of the mushy region directly in contact with the ambient air (Figure 4), two situations might arise:

(a) When the volume fraction of the solid, g_s, at a point of the surface is smaller than a critical value, $g_{s,c}$, mass feeding is supposed to occur. Therefore, the whole surface can move downward in order to compensate for shrinkage, and a Dirichlet condition, Eq. [18], ($p = p_a$) is applied. The volume of pipe shrinkage appearing at this surface is obtained by evaluating the integral of the fluid flow over the open-region boundary (Eq. [23]). This volume is distributed evenly among all the cells of the surface for which $g_s < g_{s,c}$. When all these cells are empty, a next row of cells is automatically considered, thus allowing to predict the shape of pipe shrinkage.

(b) When $g_s > g_{s,c}$ at some point, the solid is supposed to remain fixed and a homogeneous Neumann condition, Eq. [19], is imposed. (The remark already made for liquid in contact with the mold (IIa) applies here.)

Prescribing all the boundary conditions, as mentioned in (I) through (V), allows one to calculate the pressure in the liquid, p_l, the volume fraction of microporosity, g_p, and the volume of the macropores, V_p (refer to the numerical details in Section V). Furthermore, the volume of macropores is distributed among the highest cells of isolated liquid regions as solidification proceeds. Finally, at free boundaries where a Dirichlet condition is imposed (I) and (Va), the calculated pressure field allows the deduction of the velocity field at such boundaries and, thus, pipe shrinkage, *i.e.*, lowering of free surfaces. Therefore, the whole model combines microporosity, macroporosity, and pipe shrinkage calculation in a consistent way. This is done only for the cells falling in mushy elements, therefore, with a sufficient accuracy and for the domain of interest.

Finally, it should be noted that the calculation of the integral, Eq. [23], close to the liquidus has 1 to 2 pct inaccuracy because of the very wide range of permeability across the mushy zone. These errors cumulate over time. In order to respect the overall mass balance over the entire solidification process, the volume of the void is also calculated at each time-step from (Eq. [9b]):

$$\frac{\Delta V_p}{\Delta t} = a^d \sum_{i=1}^{N_c} \frac{1}{\rho_{l,i}} \frac{\Delta\langle\rho\rangle_{o,i}}{\Delta t} \qquad [24]$$

where the summation is carried out over all the mushy cells. This mass balance is then compared with the summation of microporosity, macroporosity, and pipe shrinkage volumes. The various surface integrals, Eq. [23], intervening in macroporosity and pipe shrinkage are corrected in proportion with the balance, Eq. [24], if it is necessary.

V. NUMERICAL METHOD

A macroscopic heat-transfer calculation is first performed in order to obtain the temperature and the solid fraction histories at all the nodes of the FE mesh falling in the solidifying domain. These results, interpolated for all the activated cells of the FV grid, are the input data for the porosity calculation.

The FV formulation of Eq. [9] leads to the following set of equations:

$$K_{ij}p_{lj} + M_{ii}\left[-\rho_{l,i}\frac{dg_{p,i}}{dt} + (\rho_{s,i} - \rho_{l,i})\frac{dg_{s,i}}{dt} + (1 - g_{s,i} - g_{p,i})\frac{d\rho_{l,i}}{dt}\right] - G_i = b_i \text{ for } i = 1, N_c \qquad [25]$$

where the indices i and j refer to cell locations; K_{ij} and M_{ii} are the rigidity and (diagonal) mass matrices, respectively; G_i is the contribution of gravity; and b_i the term obtained from boundary conditions (implicit summation over repeated indices has been assumed). For the time discretization, the following implicit scheme has been used in order to avoid an instability-driven limitation of the time-steps:

$$K_{ij}p_{lj}^{n+1} + M_{ii}\left[-\rho_{l,i}\frac{g_{p,i}^{n+1} - g_{p,i}^{n}}{\Delta t} + (\rho_{s,i} - \rho_{l,i})\frac{\Delta g_{s,i}}{\Delta t} + (1 - g_{s,i} - g_{p,i})\frac{\Delta\rho_{l,i}}{\Delta t}\right] - G_i = b_i \qquad [26]$$

$$\text{for } i = 1, N_c$$

The last two terms in the square brackets are obtained from the thermal calculation (shrinkage) and specific mass variation. Therefore, two unknown fields, $\{p_{l,i}\}$ and $\{g_{p,i}\}$, have to be calculated from Eq. [26] and by applying the model of segregation/precipitation of gas (Section III). Because these two fields are related locally for each cell but through nonlinear functions, the system is nonlinear. In order to linearize the function $g_{p,i}(p_{l,i}, T_i, g_{s,i})$, one iteration of Newton's method is performed for each node.[6]

$$g_{p,i}^{n+1} = g_{p,i}^{n} + \left[\frac{\partial g_p}{\partial p_l}\right]_i^n (p_{l,i}^{n+1} - p_{l,i}^{n}) + \left[\frac{\partial g_p}{\partial T}\right]_i^n (T_i^{n+1} - T_i^{n}) + \left[\frac{\partial g_p}{\partial g_s}\right]_i^n (g_{s,i}^{n+1} - g_{s,i}^{n}) \qquad [27]$$

The first derivatives of g_p, with respect to p_l, T, and g_s are calculated analytically from Eq. [12] and using the related

equations, such as Sieverts' and Laplace's laws (Eqs. [13] and [14]). The linear system obtained in this way can be rewritten as

$$A_{ij}p_{l,j} = f_i \quad \text{for } i = 1, N_c \qquad [28]$$

where A_{ij} is the matrix of the system, and f_i is the RHS term. This system is solved using a preconditioned variant of the Bi-Conjugate Gradients method.[24]

As soon as a partially closed liquid region appears during solidification, the linear system is modified because of the presence of a new variable, p_Q, and of a new equation corresponding to the formulation of the IBC, Eq. [22]. For the cell located at *Q*, the formulation of the IBC over the whole boundary gives one equation in which p_Q is the unknown. For any other cell, *R*, located at the boundary, where the unknown pressure p_R is related to p_Q, the corresponding equation is simply: $p_R - p_Q = \rho_l g h_{RQ}$, where h_{RQ} is the height separating these two cells.

VI. RESULTS AND DISCUSSION

Several test cases of increasing complexity are presented in this section. First, a 1-D situation is considered in order to validate the implementation of the IBC for partially closed liquid pockets. Then, several 2-D calculations are performed in order to illustrate the effects of various parameters and to verify the accuracy of the model. Finally, a 3-D situation with a large number of cells clearly shows the efficiency of the algorithms. The 2-D and 3-D versions of microporosity formation have been implemented in the corresponding versions of the software CALCOSOFT,* this later being used to perform the thermal calculations. This FE method software was also modified to handle the cell definition, and visualization of porosity results.

*The software CALCOSOFT, a joint development of the Ecole Polytechnique Fédérale de Lausanne and Calcom SA, Switzerland, is dedicated to the 2-D/3-D modeling of continuous processes, such as continuous casting, direct-chill casting, strip casting, as well as of advanced solidification processes.

In order to test the IBC (IIIa), the 2-D model was first applied to a 1-D thermal situation, neglecting microporosity formation (Figure 5). For that purpose, a very narrow domain was selected with appropriate thermal boundary conditions at the lateral surface. Cooling conditions on the lateral side were chosen in order to obtain a partially closed liquid pocket located in between two mushy zones. The transverse Biot number, *i.e.*, the product of the heat-transfer coefficient and transverse dimension of the domain, divided by the thermal conductivity of the alloy, was very small to ensure a nearly uniform temperature across the width. The thermal boundary conditions at both ends of this 1-D domain were adiabatic. The gray levels at the top of Figure 5 indicate the amount of solid according to the scale on the right. For the pressure drop calculation, it was assumed that no liquid could flow on the lateral sides of the domain and on the left (*i.e.*, mold). On the right boundary, a Dirichlet boundary condition was applied, and gravity was assumed to be horizontal, toward the left. For the sake of simplicity, the specific masses of the solid and liquid were assumed to be constant but different. Calculations of the pressure drop in the domain were performed with and without introducing a cavitation pressure.

When no cavitation pressure is introduced (dashed curve of Figure 5), the pressure first increases from the atmospheric pressure in the open-liquid pocket because of the metallostatic contribution. The pressure drop in the first mushy zone is such that the liquid velocity entering the partially closed liquid pocket exactly compensates for shrinkage in the second mushy zone near the mold (left boundary). The pressure in this cavity, unknown at the beginning, is around 70 kPa at the highest point (with respect to gravity) and also increases with depth. Setting up a cavitation pressure of 80 kPa (continuous curve) shifts the pressure profile upwards to this value. As a consequence, the amount of liquid flowing from the open cavity will be lowered, while solidification shrinkage in the mushy zone is the same. Therefore, the mass balance given by Eq. [23] directly gives the volume of the macropore that appears in the partially closed liquid region. The amount of liquid flowing from the right boundary is also lowered, but one clearly sees the difficulty in predicting the amount of pipe shrinkage from the integral (Eq. [23]) applied to the liquidus position on the right. The pressure profiles of the dashed and continuous curves are nearly identical because the permeability in this region is very large. This is why it is necessary to correct such integral(s) with the help of the overall mass balance (Eq. [24]).

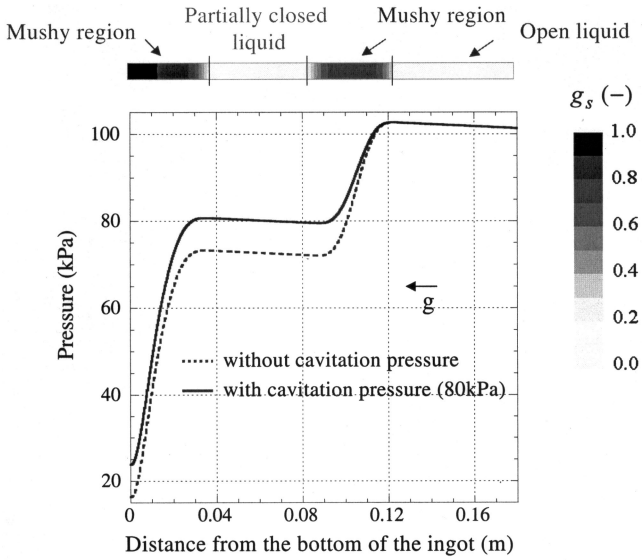

Fig. 5—1-D test of the IBC implemented for the pressure in partially-closed liquid regions.

In all the 2-D and 3-D examples that are shown hereafter, the volume fraction of microporosity is indicated with the help of a yellow-green palette, whereas macroporosity and pipe shrinkage are indicated by orange and red colors. The scale of the first palette is given for each figure, while orange and red mean 0 to 50 pct and 50 to 100 pct volume fraction of void, respectively. Moreover, the amount of hydrogen is set to 0.15 $cc_{STP}/100$ g* of metal unless it is explicitly given.

*For aluminum alloys, 0.1 cm^3 of hydrogen at standard conditions of pressure and temperature in 100 g of metal corresponds roughly to 1 ppm.

The first 2-D example shown in Figure 6 has been inspired by the A1-4.5 wt pct Cu sand-mold casting calculated by Kubo and Pehlke.[4] For the heat-flow simulation, a uniform heat-transfer coefficient of 42 W m^{-2} K^{-1} was imposed at all the sand-metal boundaries, and an adiabatic condition

Table I. Material Properties for the Various Test Cases Shown in Figures 6 through 10

	Al-4.5 wt pct Cu	Al-7 wt pct Si	Al-11 wt pct Si	
σ_{sl}	1×10^{-1}	1×10^{-1}	1×10^{-1}	J m^{-2}
D_l	5×10^{-9}	5×10^{-9}	5×10^{-9}	m^2 s^{-1}
T_M	660	660	660	°C
L	1×10^9	9.5×10^8	9.5×10^8	J m^{-3}
k	0.173	0.132	0.132	—
m	−3.434	−6.64	−6.64	K (wt pct)$^{-1}$
g_e	0.09	0.51	0.85	—
σ_{lg}	9×10^{-1}	9×10^{-1}	9×10^{-1}	J · m^{-2}
r_0	1×10^{-5}	1×10^{-5}	1×10^{-5}	m
n_0	1×10^9	1×10^9	1×10^9	m^{-3}
$\rho_{l,0}$	2440	2380	2380	kg m^{-3}
ρ_s	2620	2520	2520	kg m^{-3}
ρ_e	3400	2520	2520	kg m^{-3}
β_T	1.24×10^{-4}	—	—	°C^{-1}
β_c	-1.09×10^{-2}	—	—	(wt pct)$^{-1}$
$c_{l,0}$	4.5	7.0	11.0	wt pct
μ_0	5.36×10^{-4}	5.36×10^{-4}	5.36×10^{-4}	Pa s
E_μ	1.65×10^4	1.65×10^4	1.65×10^4	J mole^{-1}
e_H^{ci}	3×10^{-2}	3×10^{-2}	3×10^{-2}	—
r_H^{ci}	-4×10^{-4}	-8×10^{-4}	-8×10^{-4}	—

$R = 8.3144$ J mole^{-1} °C^{-1}

$\alpha = 269 \dfrac{\text{cc}_{\text{STP}}\text{H}_2}{100\text{ g}}$ K s^2 m^{-2}

was applied to the top free surface of this L-shaped casting. The other conditions and parameters are indicated in Table I. Figure 6 represents the final amount of porosity in the casting for two different nominal concentrations of hydrogen with and without pipe shrinkage. In Figure 6(a), the amount of hydrogen is 0.15 cc_{STP}/100 g of metal, and the top surface of the L-shaped casting is supposed to be connected to a riser (but the metallostatic head of the riser is neglected). Since the casting is well fed, the amount of microporosity is fairly limited (around 0.5 pct or lower). Under exactly the same conditions, a doubling of the initial concentration of hydrogen (Figure 6(b)) more than doubles the amount of microporosity (as much as 1.1 pct). As already noted by Rousset *et al.*,[22] microporosity must first offset the undersaturation of the melt and then overcome the nucleation barrier (Figure 1). Keeping the concentration of hydrogen at 0.15 cc_{STP}/100 g but assuming now that the top surface is not connected to a riser (Figure 6(c)) leads to a very large pipe-shrinkage cavity: the shape of which is dictated by that of the isotherm when $g_s = g_{s,c}$. The amount as well as the distribution of microporosity are also completely different. The largest amount of microporosity is no longer found near the end of the casting but close to the bottom of the pipe shrinkage. Such behavior seems in agreement with usual casting practices and results obtained by Kubo and Pehlke.[4]

The second 2-D example, shown in Figure 7, illustrates the influence of the grain structure on the amount of microporosity, macroporosity, and pipe shrinkage for an A1-4.5 wt pct Cu Y-shaped casting. The mold is assumed to be around the whole component, except on the left-top surface of the Y shape (gravity is downward). The parameters being given in Table I, two calculations have been performed by just changing the value of the critical volume fraction of solid, $g_{s,c}$, above which a free surface is assumed to remain fixed. For columnar structure growing from the side of the mold (Figure 7(a)), the value of $g_{s,c}$ has been set to zero and feeding can only occur from the portion of the top surface that is fully liquid. As a consequence, feeding of the mushy zone becomes difficult early during solidification, and a macroshrinkage cavity forms within the casting. At the same time, pipe shrinkage is limited, while the amount of microporosity is high (between 8 and 10 pct). With the assumptions presently made, no pipe shrinkage is predicted near the right-top surface of the Y-shaped casting. It is equivalent to assuming that the mold is impermeable to air, which might not be true. However, such hypothesis could be relaxed by setting an appropriate pressure at this surface (Dirichlet condition) instead of a Neumann condition. Assuming now that the alloy was inoculated and equiaxed grains form, mass feeding can occur, *i.e.*, the free surface can move downward even if the melt is already mushy. Setting arbitrarily the value of $g_{s,c}$ to 0.2 (Figure 7(b)), one can see that feeding is much more effective. The macroshrinkage cavity has disappeared, microporosity has been reduced, but pipe shrinkage is much more pronounced. In both cases, the total void formation (*i.e.*, cumulated volume of microporosity, macroporosity, and pipe shrinkage) is equal to 8.33×10^{-4} m^2, which corresponds to the overall solidification shrinkage of the alloy (10.25 pct, Table I, volume of the casting equal to 8.05×10^{-3} m^2).

In order to test the sensitivity of the model to solute concentration, the third 2-D example, shown in Figure 8, corresponds to the solidification of A1-7 wt pct Si (AS7) and A1-11 wt pct Si (AS11) alloys in a 2-D axisymmetric geometry. Again, this dummy blade is supposed to be surrounded by the mold everywhere, except at the top free surface where the atmospheric pressure is imposed. The two calculated results have been mounted in a symmetric fashion so as to clearly reveal the differences induced solely by the alloy concentration; all the other parameters having been kept identical. As can be expected from the extent of the mushy zones of these two alloys, the amount of microporosity in the AS7 casting is greater than in the AS11 one. Concomitantly, the cavitation pressure is reached at the mid-height horizontal platform of the dummy blade during the solidification of the AS7 alloy, while some liquid remained. As a result, a macroporosity has formed near the upper surface of this platform, which is not the case for the AS11 alloy. This example also demonstrates that the model can account for macrocavity forming near (or at) an internal surface, which is still liquid. On the other hand, the critical solid fraction $g_{s,c}$, being and equal to 0.2, pipe shrinkage in AS11 is larger than in AS7; the total volume of void in the two castings remaining nearly the same (2.6×10^{-5} m^3).

The last 2-D example (Figure 9) demonstrates the ability of the model to handle multiple liquid pockets and shows the influence of the metallostatic pressure and cooling conditions on the final microporosity and macroporosity. In this cross-shaped casting, only the top free surface is exposed to air. The upper square volume is, therefore, the only part that can feed three other volumes labeled A, B, and C. Gravity being downward, the metallostatic head of cavities A and B is the same, while it is larger for cavity C. Cooling conditions of cavities B and C are the same (heat-transfer coefficient equal to 5 Wm^{-2}K^{-1}), whereas cavity A is cooled faster (10 Wm^{-2}K^{-1}). Cooling conditions on the narrow

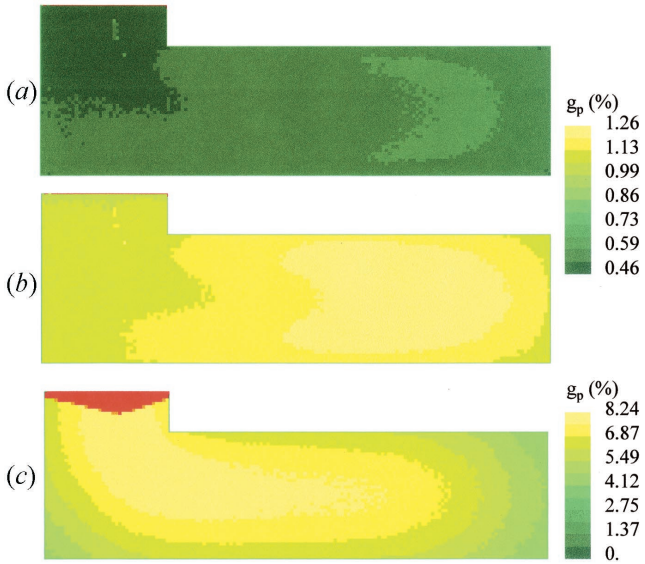

Fig. 6—Influence of the nominal concentration of gas (*a* and *b*) and of the absence of a riser (*c*) connected to the top surface on the microporosity level and pipe shrinkage in a L-shape Al-4.5 wt pct Cu sand mold casting (conditions in Table I).

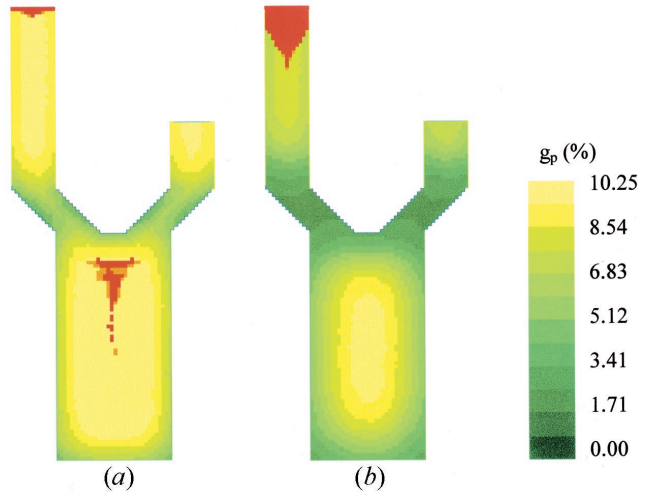

Fig. 7—(*a*) and (*b*) Influence of the microstructure *via* the critical volume fraction of solid, $g_{s,c}$, on the final microporosity, macroporosity, and pipe shrinkage in a Y-shape Al-4.5 wt pct Cu sand mold casting (conditions in Table I).

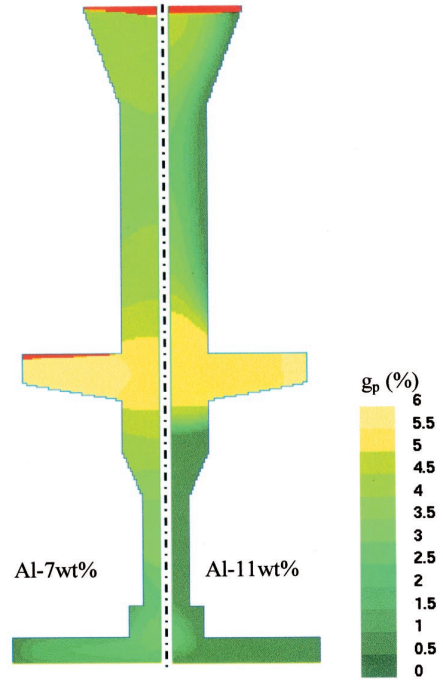

Fig. 8—Influence of the alloy concentration on the final microporosity, macroporosity, and pipe shrinkage in a dummy axisymmetric turbine blade of Al-Si alloys (conditions in Table I).

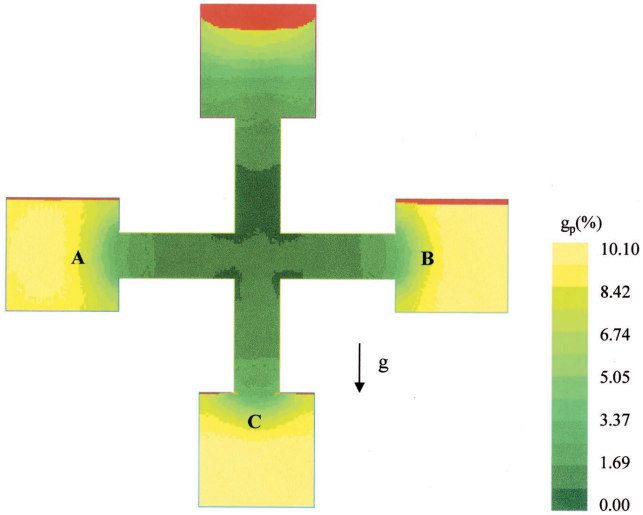

Fig. 9—Influence of the metallostatic pressure and cooling conditions on the final microporosity, macroporosity, and pipe shrinkage in a cross-shape Al-4.5 wt pct Cu alloy (conditions in Table I).

sections of the cross-shaped casting are dictated by a heat-transfer coefficient of 150 $Wm^{-2}K^{-1}$. Although these cooling conditions are quite far from experiments, the result shown in Figure 9 clearly indicates that an increased metallostatic head simply delays the formation of macroporosity (compare cavities B and C) and reduces its final volume. Comparing now cavities A and B (same metallostatic head), the macroporosity developing in A is reduced, as the liquid in this region is cooled faster and feeding is more efficient. Please note the important volume of pipe shrinkage in the upper part of the cross-shaped casting.

To conclude this section, Figure 10 shows the case of a real 3-D casting of 4.3 m^3. Although this casting was originally made in steel, it was replaced in the present case by an A1-4.5 pct Cu alloy. The casting having a plane of symmetry, only half was modeled. The two extreme risers were cut by the plane of symmetry, while the two central ones were not. Figures 10(a) and (b) show the temperature and solid fraction repartitions at a given time in the casting, with the corresponding scale on the top left corner, as obtained with CALCOSOFT. The porosity model was then run with more than half-a-million cells (total CPU time of about 31 hours on a 686 PC running under Linux). Figures 10(c) and (d) show the final porosity repartition and pipe shrinkage in the casting, as calculated with the parameters given in Table I. Figure 10(c) corresponds to the surface

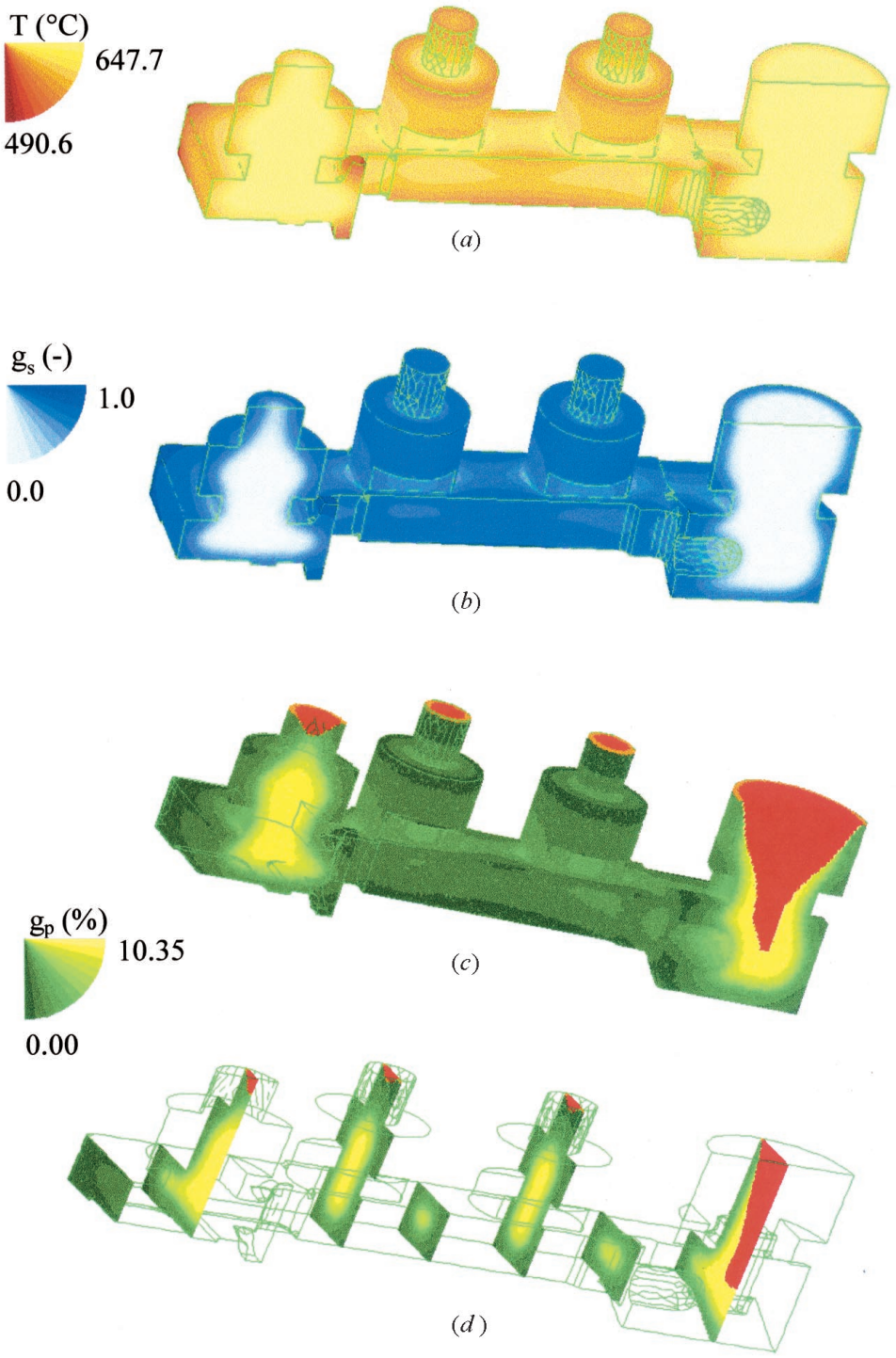

Fig. 10—(*a*) Temperature and (*b*) solid fraction repartitions at a certain time and (*c*) final microporosity level and; (*c*,*d*) pipe shrinkage in a 3-D Al-4.5 wt pct Cu casting.

and symmetry plane section, whereas Figure 10(d) corresponds to selected transverse sections. As can be seen, pipe shrinkage is very important in the extreme right riser, which has the largest volume and remains liquid for a long period of time, whereas the three other risers have moderate pipe shrinkage. There is no macroshrinkage cavity, which indicates that rigging was correctly made, and the amount of microporosity is maximum near the pipe-shrinkage holes.

VII. CONCLUSIONS

A FV model for the prediction of microporosity, macroporosity, and pipe shrinkage during the solidification of alloys has been developed for 2-D (cartesian and axisymmetric) and 3-D geometry. It includes all the basic physical phenomena, which are at the origin of microporosity. In particular, pressure drop in the mushy zone, segregation of gas, equilibrium

between gas bubbles and solid-liquid phases, laws of nucleation and growth of pores are taken into account. Pipe shrinkage and macroporosity are predicted by detecting automatically open, partially closed, and closed liquid regions and by applying appropriate boundary conditions. A mushy-zone tracking procedure has been developed in order to have a good accuracy in the mushy zone, while limiting the number of nodes and CPU time. The model seems to give the correct trend for the influence on porosity and pipe shrinkage of various parameters, such as gas content, alloy concentration, nucleation parameters, cooling conditions, and gravity. In future work, numerical results will be compared with experimental measurements.

ACKNOWLEDGMENTS

This work was performed within the framework of the CTI Project, Contract No. 3666.1. This project has been officially certified as Eureka Project No. E!2091 gaining an internationally recognized quality label of technological innovation. The financial support of Assan (Turkey), Calcom (Switzerland), Doncasters (United Kingdom), Elkem (Norway), Hydro Aluminium (Norway), Pechiney (France), Rolls-Royce (United Kingdom), Sintef (Norway), Snecma (France), VAW (Germany), and The Swiss Commission for Technology and Innovation (CTI, Bern) are gratefully acknowledged. The authors also thank S. Pellerin, V. Maronnier, and J.-F. Joyeux, Calcom, for the development of the postprocessing, cell definition modules, and integration of the present model into CALCOSOFT, respectively; J.-L. Desbiolles, EPFL, for his valuable advice and various contributions; and B. Commet, Pechiney, for a remark regarding the hydrogen mass balance.

REFERENCES

1. J. Campbell: *Castings*, Butterworth-Heinemann, 1991.
2. T.S. Piwonka and M.C. Flemings: *Trans. AIME*, 1966, vol. 236, pp. 1157-65.
3. S. Shivkumar, D. Apelian, and J. Zou: *AFS Trans.*, 1989, vol. 97, pp. 989-1000.
4. K. Kubo and R.D. Pehlke: *Metall. Trans. B*, 1985, vol. 16B, pp. 359-66.
5. M. Rappaz: in *Advanced Course in Solidification*, Calcom SA, Lausanne, Switzerland, 1996.
6. J. Ampuero, C. Charbon, A.F.A. Hoadley, and M. Rappaz: in *Materials Processing in The Computer Age*, V.R. Voller, M.S. Stachowicz, and B.G. Thomas, eds., TMS, Warrendale, PA, 1991, pp. 377-88.
7. D. Carpentier: Ph.D. Thesis, Institut National Polytechnique de Lorraine, Nancy, France, 1994.
8. D.R. Poirier, K. Yeum, and A.L. Mapples: *Metall. Trans. A*, 1987, vol. 18A, pp. 1979-87.
9. J.D. Zhu and I. Ohnaka: in *Modeling of Casting, Welding and Advanced Solidification Processes V*, M. Rappaz, M.R. Ozgu, and K. Mahin, eds., TMS, Warrendale, PA, 1991, pp. 435-42.
10. J. Huang and J.G. Conley: *Metall. Mater. Trans. B*, 1998, vol. B29, pp. 1249-60.
11. S. Bounds, G. Moran, K. Pericleous, M. Cross, and T.N. Croft: *Metall. Mater. Trans. B*, 2000, vol. 31B, pp. 515-27.
12. P.D. Lee and J.D. Hunt: *Acta Mater.*, 2001, vol. 49, pp. 1383-98.
13. P.D. Lee, A. Chirazi, and D. See: *J. Light Met.*, 2001, vol. 1, pp. 15-30.
14. P. Vo, D. Maijer, C. Hermesmann, and S.L. Cockcroft: *Light Met. 2001*, J.L. Anjier, ed., TMS, Warrendale, PA, 2001, pp. 1115-21.
15. A.S. Sabau and S. Viswanathan: *Light Metals*, TMS, Warrendale, PA, 2000, pp. 597-602.
16. M. Gremaud and M. Rappaz: *AFS Trans.*, 2002, in press.
17. N. Provatas, N. Goldenfeld, and J. Dantzig: *J. Comp Phys.*, 1999, vol. 148, pp. 265-90.
18. C.-A. Gandin, J.-L. Desbiolles, M. Rappaz, and P. Thévoz: *Metall. Trans. A*, 1999, vol. 30A, pp. 3153-65.
19. W. Kurz and D.J. Fisher: *Fundamentals of Solidification*, 4th revised edition, Trans Tech Publications, Aedermannsdorf, Switzerland, 1989.
20. M. Rappaz and W.J. Boettinger: *Acta Metall. Mater*, 1999, vol. 47, pp. 3205-19.
21. T. Kajitani, J.-M. Drezet, and M. Rappaz: *Metall. Mater. Trans. A*, 2001, vol. 32A, pp. 1479-91.
22. P. Rousset, M. Rappaz, and B. Hannart: *Metall. Mater. Trans. A*, 1995, vol. 26A, pp. 2349-57.
23. M. Rappaz: *Int. Mater. Rev.*, 1989, vol. 34, pp. 93-123.
24. S.-L. Zhang: *Siam J. Sci. Comput.*, 1997, vol. 18 (2), pp. 537-51.